Received: 23 January 2020 | Revised: 8 July 2020 | Accepted: 27 July 2020 | Published on: 9 September 2020

DOI: 10.1002/qj.3883

Quarterly Journal of the Royal Meteorological Society RMetS

RESEARCH ARTICLE

Assimilating synthetic land surface temperature in a coupled land–atmosphere model

Christine Sgoff[1,2] | Annika Schomburg[1] | Juerg Schmidli[2] | Roland Potthast[1]

[1]Deutscher Wetterdienst, Offenbach, Germany

[2]Hans-Ertel Centre for Weather Research, Goethe University Frankfurt, Germany

Correspondence
C. Sgoff, Deutscher Wetterdienst, Offenbach am Main, Germany.
Email: christine.sgoff@dwd.de

Funding information
Goethe-Universität Frankfurt am Main, Grant/Award Number: DWD2014P4

Abstract

A realistic simulation of the atmospheric boundary layer (ABL) depends on an accurate representation of the land–atmosphere coupling. Land surface temperature (LST) plays an important role in this context and the assimilation of LST can lead to improved estimates of the boundary layer and its processes. We assimilated synthetic satellite LST retrievals derived from a nature run as *truth* into a fully coupled, state-of-the-art land–atmosphere numeric weather prediction model. As assimilation system a local ensemble transform Kalman filter was used and the control vector was augmented by the soil temperature and humidity. To evaluate the concept of the augmented control vector, two-day case-studies with different control vector settings were conducted for clear-sky periods in March and August 2017. These experiments with hourly LST assimilation were validated against the nature run and overall, the RMSE of atmospheric and soil temperature of the first-guess (and analysis) were reduced. The temperature estimate of the ABL was particularly improved during daytime as was the estimate of the soil temperature during the whole diurnal cycle. The best impact of LST assimilation on the soil and the ABL was achieved with the augmented control vector. Through the coupling between the soil and the atmosphere, the assimilation of LST can have a positive impact on the temperature forecast of the ABL even after 15 hr because of the memory of the soil. These encouraging results motivate further work towards the assimilation of real satellite LST retrievals.

KEYWORDS

data assimilation, land–atmosphere coupling, land surface temperature, LETKF

1 | INTRODUCTION

The coupling between soil and atmosphere plays an important role for atmospheric boundary layer (ABL) development (Koster *et al.*, 2006; Holtslag *et al.*, 2007; Sandu *et al.*, 2013). Hence, a realistic simulation of the ABL needs an accurate representation of the thermal coupling and the surface processes (Reichle *et al.*, 2010; Bosveld *et al.*, 2014; Trigo *et al.*, 2015). It is well-known that the energy budget

at the surface depends on long- and short-wave radiation, sensible and latent heat flux, and soil heat flux. The land surface temperature (LST) is a crucial part of this surface energy budget. For instance, LST plays a role in the partitioning of sensible and latent heat flux and determines the upward thermal radiation. Therefore, improving the representation of LST in atmospheric simulations has the potential to further enhance the representation of variables and fluxes that are correlated with LST (Bosilovich *et al.*, 2007; Santanello *et al.*, 2013; Trigo *et al.*, 2015; Candy *et al.*, 2017).

The initial state of the land surface and the boundary layer affects the time evolution of the boundary layer. The combination of information from observed and simulated land surface observations/fields, can produce a more representative estimate of land surface conditions and boundary-layer processes (Margulis and Entekhabi, 2003; Ghent *et al.*, 2010; Reichle *et al.*, 2010; Han *et al.*, 2013). Therefore, the assimilation of LST into a fully coupled land–atmosphere model is expected to lead to improvements in initial LST and in the forecasts of correlated variables like surface fluxes. A comprehensive LST retrieval can be derived from remote-sensing observations (Aires *et al.*, 2004; Jin, 2004; Trigo *et al.*, 2008). Geostationary satellites measure with a high temporal resolution and are thus able to resolve the full diurnal cycle of LST. Measurements of the Spinning Enhanced Visible and InfraRed Imager (SEVIRI) on board Meteosat Second Generation (MSG) provide a spatial resolution of $\Delta x \approx 5$ km over central Europe at a temporal resolution of $\Delta t = 15$ min (Trigo *et al.*, 2008) and thus offer a promising option for LST assimilation.

Several efforts have been made to assimilate LST retrievals in land surface models to improve the surface energy budget and the representation of land surface properties. Huang *et al.* (2008) combined LST assimilation and a leaf area index (LAI) update in a single-column land model, which led to an improved profile of the modelled soil temperature. Reichle *et al.* (2010) assimilated real LST observations in two different land surface models, which led to improved LST in both models. A further study with real LST derived from the SEVIRI instrument was carried out by Ghent *et al.* (2010). The assimilation of LST into the land surface model led to better simulated LST and soil moisture, as well as sensible and latent heat fluxes. Han *et al.* (2013) realised a joint assimilation of synthetic LST and microwave brightness temperature into a land model. Different impacts on the profiles of soil temperature and soil moisture were found. Under dry conditions the assimilation of LST resulted in an improved soil moisture characterization. Pinjosovsky *et al.* (2017) carried out LST assimilation to improve the estimation of land surface model parameters. By estimating the parameters most sensitive to LST, they were able to improve the forecast of surface fluxes.

All these studies investigated the effect of LST assimilation on stand-alone land surface models. There are also some studies which investigate the impact of LST assimilation on atmospheric models or atmospheric boundary-layer models. First steps in this direction were made by McNider *et al.* (1994). They assimilated skin temperature tendencies into a boundary-layer model in order to get a LST estimate closer to LST retrievals from satellites. Margulis and Entekhabi (2003) applied a variational approach to assimilate standard reference-level temperature and humidity, and radiometric surface temperature measurements into a coupled single-column land surface–atmospheric boundary-layer model. Tests with the single-column model were able to supply more accurate estimates of the land surface fluxes. A variational approach was also used by Tajfar *et al.* (2020b). They successfully combined the assimilation of LST into the soil heat diffusion equation (Bateni *et al.*, 2013a; 2013b) with the assimilation of reference-level air temperature and specific humidity into an ABL model (Tajfar *et al.*, 2020a) and were also able to improve the land surface fluxes. Bosilovich *et al.* (2007) provided an incremental bias correction scheme for LST. The bias corrected term was assimilated into the land surface energy budget of a land surface model. This led to an enhancement of skin temperature as well as of sensible and latent flux. In addition, the skin temperature was used as a lower boundary condition for an atmospheric model. A positive impact was also found on atmospheric variables like near-surface air temperature. Candy *et al.* (2017) assimilated LST into a land surface model. The effect on a numerical weather prediction (NWP) model was investigated by using the updated soil temperature and moisture as forcing for the next NWP model forecast. It was found that the amount of improvement through LST assimilation was dependant on the land cover type. Generally, improvements in near-surface air temperature over Europe and Africa could be achieved.

In conclusion, many studies have shown a beneficial impact on LST and on the soil state through LST assimilation, and some also on the atmosphere through indirect effects of an improved soil state.

To investigate the simultaneous direct and indirect effect of LST assimilation on the ABL and its processes, a coupled land–atmosphere LST assimilation system is employed in the current study. The LST assimilation is performed within a state-of-the-art NWP system as an Observing System Simulation Experiment (OSSE). The synthetic LST observations emulate retrievals from the SEVIRI instrument (Section 3.2) and are assimilated into the COnsortium for Small-scale MOdelling (COSMO)

model (Section 2.1). The data assimilation scheme used is the Kilometre-scale ENsemble Data Assimilation scheme (KENDA; Section 2.2), which is based on the Local Ensemble Transform Kalman Filter (LETKF; Hunt *et al.*, 2007). By extending the LETKF control vector to soil variables, the simultaneous LST assimilation into the land and the atmosphere module of the COSMO model is realised. In this way LST assimilation has a direct impact on the soil and the atmosphere and an indirect effect through interaction between the adjusted land and the atmosphere. Single-observation experiments (Section 4.1) and impact studies with different control vector set-ups (Section 4.2) are performed over a domain in northeastern Germany (Section 3.1). The conclusions are presented in Section 5.

2 | MATERIALS AND METHODS

2.1 | The COSMO model

The COSMO model is a non-hydrostatic regional model (Baldauf *et al.*, 2011b). It is maintained by the Consortium for Small Scale Modelling (COSMO; http://www.cosmo-model.org/; accessed 13 August 2020), a group of meteorological services from Germany, Greece, Israel, Italy, Poland, Romania, Russia, and Switzerland. In this study, COSMO version 5.04c with most settings equal to the formerly operational COSMO-DE at Deutscher Wetterdienst (DWD, German Weather Service) is used (Baldauf *et al.*, 2011a). Prognostic model variables include a three-dimensional wind vector, temperature, pressure (deviation from a reference state), turbulent kinetic energy (TKE) as well as specific contents of the different precipitation types: water vapour, cloud water, cloud ice, rain, snow, and graupel. The prognostic equations are solved on an Arakawa C-grid and the coordinate system has rotated geographical coordinates with a generalised terrain-following height coordinate. The atmosphere is represented by 50 layers of a hybrid grid with terrain-following layers close to the surface of the Earth and horizontally flat model layers in the stratosphere. The horizontal resolution of the model grid is 2.8 km. With this resolution, deep moist convection is assumed to be explicitly resolved.

The COSMO model includes a multi-layer soil and vegetation model (TERRA_ML; Doms *et al.*, 2011; Schulz *et al.*, 2016). The thermal module of the soil has seven active layers with increasing thickness of 0.01, 0.03, 0.09, 0.27, 0.81, 2.43 and 7.29 m below the surface and an inactive climate layer as a constant lower boundary at 21.78 m depth. The temperature of the climate layer is the annual mean near-surface temperature. The annual temperature amplitude is already quite small at 7.29 m, hence a constant temperature below this depth may be safely used. The hydrological module of the soil has only six active layers with the same layer structure as the thermal module. The lowest hydrological layer at a depth of 2.43 m accounts only for the downward gravitational transport, which contributes to the runoff (Schrodin and Heise, 2002).

In the COSMO model the energy budget at the surface is both the lower boundary condition for the atmosphere and the upper boundary condition for the soil. The surface energy budget is given by

$$Q_{\text{net}} = G_{\text{sfc}} + H + L, \tag{1}$$

and determines the partitioning of the net available energy Q_{net}, into the sensible heat flux H, the latent heat flux L, and the ground heat flux G_{sfc}. Within the surface energy budget, LST is a diagnostic variable T_{surf} of weighted temperatures over land. LST consists of the snow surface temperature T_{snow} and the skin-layer temperature T_{skin} over snow-free areas

$$T_{\text{surf}} = \alpha_{\text{snow}} T_{\text{snow}} + (1 - \alpha_{\text{snow}}) T_{\text{skin}}, \tag{2}$$

where α_{snow} is the fraction of the snow cover. In the implementation used for this study, the skin layer temperature T_{skin} replaced the bare soil surface temperature T_{s} used operationally (Schulz and Vogel, 2020). It is defined as the temperature of a skin layer with no heat capacity above the soil (Viterbo and Beljaars, 1995). The layer simulates the shading effects of vegetation and is defined by the skin conductivity Λ_{skin}. The skin conductivity is a conceptual value and provides the thermal connection between the skin level and soil surface based on Fourier's Law:

$$G_{\text{sfc}} = \Lambda_{\text{skin}} (T_{\text{skin}} - T_{\text{s}}). \tag{3}$$

Within this study, the skin conductivity is assumed as a constant value of $\Lambda_{\text{skin}} = 10\,\text{W}\cdot\,\text{m}^{-2}\cdot\text{K}^{-1}$ (Schulz and Vogel, 2020).

The surface turbulent fluxes are determined by a standard bulk-aerodynamic approach. The sensible heat flux H is defined by

$$H = -\rho c_p C_{\text{h}}^{\text{d}} |\mathbf{v}_{\text{h}}| (T - T_{\text{skin}}) \,, \tag{4}$$

where C_{h}^{d} is the bulk-aerodynamic transfer coefficient for turbulent heat exchange at the surface, ρ is the density of air, c_p is the heat capacity, and $\mathbf{v}_{\text{h}} = (u^2 + v^2)^{1/2}$ is the absolute wind speed at the lowest atmospheric level above the surface with u and v as horizontal wind velocity

components at this level. The latent heat flux L is also part of the surface layer parametrization

$$L = -\rho L_v C_d^q |\mathbf{v}_h| (q^v - q^v_{skin}) \, . \tag{5}$$

Here, C_d^q is the bulk-aerodynamic coefficient for turbulent moisture transfer at the surface, L_v is the specific latent heat, q^v is the specific humidity at the lowest atmosphere level above the surface, and q^v_{skin} is specific humidity at the ground level and is predicted by the soil and vegetation model TERRA_ML. The computation of evapotranspiration is divided in bare soil evaporation (Schulz and Vogel, 2020) and transpiration from plants (Noilhan and Planton, 1989). The net long- and short-wave radiation at the land surface Q_{net} is derived with the so-called δ-two-stream radiation scheme after Ritter and Geleyn (1992) modelling the full cloud–radiation feedback.

2.2 | Assimilation framework

Ensemble Kalman Filters (EnKFs) are a common technique for data assimilation (Evensen, 1994). Within EnKFs the analysis ensemble is derived from the background ensemble. This is an efficient approach, because the background-error covariance matrix update $\mathbf{P}^b$ is calculated from the background-ensemble perturbations:

$$\mathbf{P}^b = (k-1)^{-1} \mathbf{X}^b (\mathbf{X}^b)^T \, . \tag{6}$$

k is the ensemble size and the k columns of the $\mathbf{X}^b$ matrix represent the deviations of the background-ensemble members $\mathbf{x}^{b(i)}$ from the background-ensemble mean $\overline{\mathbf{x}}^b$

$$\mathbf{X}^{b(i)} = \mathbf{x}^{b(i)} - \overline{\mathbf{x}}^b \, . \tag{7}$$

In this study the COSMO-KENDA implementation (Schraff *et al.*, 2016) based on the LETKF (Hunt *et al.*, 2007) is used. The LETKF transforms most calculations to the k-dimensional ensemble space (Hunt *et al.*, 2007). This is done to gain computational efficiency compared to calculations in the higher dimensional physical space. To find the best-fitting state, a so-called cost function is minimized on each analysis grid point (Hunt *et al.*, 2007; Szunyogh *et al.*, 2008). The cost function in ensemble space is formulated as

$$J(\mathbf{w}) = (k-1)(\mathbf{w}^T \mathbf{w}) + (\mathbf{y}^o - \overline{\mathbf{y}}^b - \mathbf{Y}^b \mathbf{w})^T \mathbf{R}^{-1} (\mathbf{y}^o - \overline{\mathbf{y}}^b - \mathbf{Y}^b \mathbf{w}), \tag{8}$$

where $\mathbf{w}$ is the k-dimensional state vector with the corresponding model state vector $\mathbf{x}$ given by

$$\mathbf{x} = \overline{\mathbf{x}}^b + \mathbf{X}^b \mathbf{w} \tag{9}$$

(Hunt *et al.*, 2007). $\mathbf{R}$ is the observation-error covariance matrix, and $\mathbf{y}^o$ is the observation vector. To allow for a non-linear observation operator, a linear approximation of the observation operator H is applied

$$H(\overline{\mathbf{x}}^b + \mathbf{X}^b \mathbf{w}) \approx \overline{\mathbf{y}}^b + \mathbf{Y}^b \mathbf{w} \, , \tag{10}$$

According to this, the ensemble of background observation members is defined by $\mathbf{y}^{b(i)} = H(\mathbf{x}^{b(i)})$ and $\overline{\mathbf{y}}^b$ is the background observation mean. The k columns of $\mathbf{Y}^b$ represent the deviations between $\mathbf{y}^{b(i)}$ and $\overline{\mathbf{y}}^b$. If the cost function (8) is minimized by $\overline{\mathbf{w}}^a$

$$\overline{\mathbf{w}}^a = \mathbf{P}^a (\mathbf{Y}^b)^T \mathbf{R}^{-1} (\mathbf{y}^o - \overline{\mathbf{y}}^b) \tag{11}$$

with

$$\mathbf{P}^a = [(k-1)\mathbf{I} + (\mathbf{Y}^b)^T \mathbf{R}^{-1} \mathbf{Y}^b]^{-1}, \tag{12}$$

then the cost function in physical space is minimized by

$$\overline{\mathbf{x}}^a = \overline{\mathbf{x}}^b + \mathbf{X}^b \overline{\mathbf{w}}^a \, . \tag{13}$$

In addition to the 40 ensemble members, the KENDA-system also includes a deterministic run employing the Kalman gain matrix from the LETKF (Schraff *et al.*, 2016). The deterministic run provides a better representation of clouds and cloud-related variables than the ensemble mean with smoothed fields of cloud-related variables due to the averaging. The analysis $\mathbf{x}^a_{det}$ of the deterministic assimilation cycle is calculated by:

$$\mathbf{x}^a_{det} = \mathbf{x}^b_{det} + \mathbf{K}\{\mathbf{y}^o - H(\mathbf{x}^b_{det})\}. \tag{14}$$

The Kalman gain matrix for the ensemble mean $\mathbf{K} = \mathbf{X}^b \mathbf{P}^a (\mathbf{Y}^b)^T \mathbf{R}^{-1}$ is applied to the difference between observations and deterministic first-guess.

To avoid spurious correlations, spatial localisation is implemented. This means that the local analysis has different weight matrices for each grid point, thus only nearby observations are taken into account. The observations are scaled by the Gaspari–Cohn correlation function (Gaspari and Cohn, 1999) with different localisation radii in the horizontal and the vertical directions. The optimal localisation depends on the observation density, quality, and representativity. Here, the horizontal localisation-scale is set to a constant value of 5.5 km, which equals a localisation radius of about 20 km. A coupled assimilation system is set up by including the soil temperature and the soil moisture

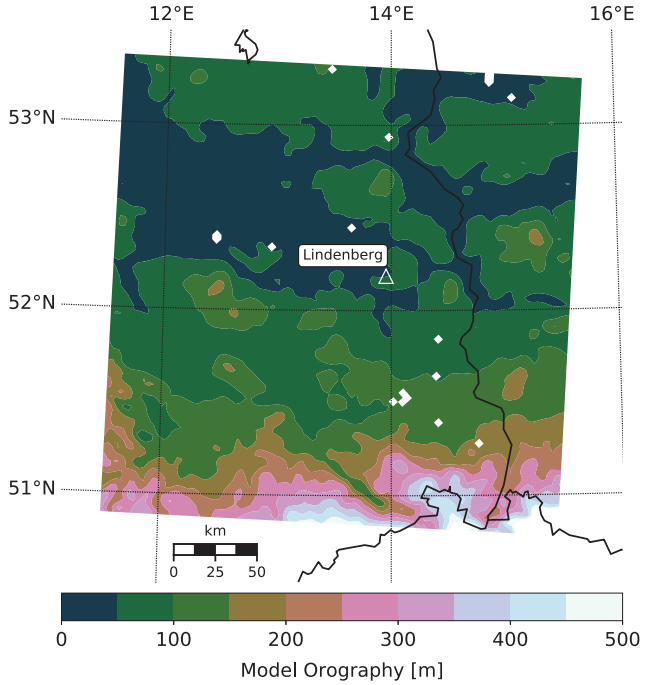

FIGURE 1 Model domain around Lindenberg observatory. The model terrain height is mainly close to sea level; only in the southeastern part of the domain are there some mountains (elevation up to 1,200 m). White areas denote lakes

into the control vector in addition to the operational set of atmospheric variables. The vertical localisation in the soil is implemented as well by the Gaspari–Cohn correlation function (Gaspari and Cohn, 1999), here with a localisation-scale set to 0.2 m. The computation of the weight matrices is performed on a three times coarser analysis grid and spatially interpolated onto the fine model grid. The vertical coarse analysis grid of the atmosphere has 35 pressure levels with a higher density close to the surface, that is, the experiments are more highly resolved than the operational set-up with 30 vertical analysis levels.

3 | EXPERIMENTAL SET-UP

3.1 | Experimental area and periods

The experimental area is located in the northeastern part of Germany including small parts of Poland and the Czech Republic (Figure 1). In the centre of the area, the Lindenberg observatory, a DWD measurement site, is situated. The experimental area has heterogeneous surface properties, the southwestern part of the area is mainly an agricultural region with the remainder being covered by forest.

The main limitation of any satellite LST retrieval availability is cloud cover. Thus two clear-sky periods in 2017 are chosen for the experiment: an early spring period from 25 to 29 March, when a large high-pressure system was situated over Europe which resulted in several clear-sky days, and a clear-sky summer period from 26 to 30 August.

3.2 | Nature run and synthetic LST

Within this study a so-called nature run is carried out in order to derive synthetic LST observations. The nature run is assumed to be the *true* state of the atmosphere and soil during the study period. Besides the generation of synthetic LST observations, the nature run is also used to evaluate the impact of the LST assimilation. The synthetic LST used within this study emulates the LST retrieval derived by the Land Surface Analysis Satellite Application Facility (Land SAF; Trigo *et al.* (2011)).

The nature run is realised with the COSMO model on the model domain (Section 3.1) with a horizontal resolution of 700 m, a resolution four times greater than for COSMO-DE, the model used within the assimilation framework. To deal with the higher resolution, the turbulence and the radiation schemes are adapted. This means that the radiation scheme is called every three forecast minutes – five times more frequently than in the operational COSMO-DE set-up – and the TKE-based turbulence parametrization takes into account the TKE advection and the horizontal diffusion of TKE (based on Blahak 2015). The initialisation and the boundary conditions are obtained from the COSMO-DE analysis interpolated onto the 700 m grid.

To mimic the LST derived from SEVIRI, an appropriate model equivalent of the COSMO model is used (Equation (2)). The model equivalent from the nature run is averaged to the satellite resolution of the real observations. Areas with a cloud cover greater than 10% and lakes are not taken into consideration (Section 3.1) because in these areas no observations would be available in a real set-up. Measurement noise is added to the synthetic LST by a random Gaussian perturbation in the range of the real observation error of 1 to 2 K (Trigo *et al.*, 2008; Freitas *et al.*, 2010; Göttsche *et al.*, 2013).

3.3 | Experimental set-up of the coupled system assessment

Two different types of experiment were conducted to evaluate the coupled system: single-observation experiments (Section 4.1) and two-day LST assimilation case-studies with different control vector settings (Section 4.2). Both types of experiment were based on a 40-member ensemble, which was initialised with and driven by the ICON-EU

TABLE 1 Experiments with different control vector settings

Experiment	Control Vector
Control	No assimilation
EXPatmos	Atmosphere
EXPsoil	Soil
EXPatso	Atmosphere and soil

ensemble (ICOsahedral Non-hydrostatic model; Zängl *et al.*, 2015). The ICON-EU ensemble has a horizontal resolution of 6.5 km. Therefore, a "spin-up" period of two days was chosen, to receive ensemble perturbations on the small scale. During the spin-up from 25 March 0000 UTC to 27 March 0000 UTC and from 26 August 1200 UTC to 28 August 1200 UTC respectively, real observations (i.e., measurements of radiosonde ascents, aircraft observations, 10 m winds, and surface pressures) were assimilated to gain a realistic difference between the nature run and the ensemble. Thus, the assimilation cycle of the early spring period started at 0100 UTC on 27 March and the assimilation cycle of the summer period started at 1300 UTC on 28 August. To avoid boundary effects, a boundary of ten grid points, corresponding to 28 km, was omitted in the following evaluation (Section 4). The assimilation cycle was based on an hourly assimilation of LST, that is, the first-guess equalled a 1 hr forecast.

To see how the augmented COSMO-KENDA system works and how the effect of LST assimilation varies during the diurnal cycle, the Single-Observation Experiments (SOEs) were carried out on 27 March and 29 August at 0000 UTC (0200 h local time) and 1200 UTC (1400 h local time). In the SOEs, 35 grid points evenly distributed over the experiment domain were chosen and the nearest synthetic LST retrieval was assimilated once. The operationally used control vector was augmented by the soil temperature and soil moisture. To guarantee a SOE set-up for each observation, the localisation scale is 5.5 km and the observations are at least 35 km apart. The impact of the LST assimilation was investigated by atmospheric and soil temperature profiles and correlation profiles. To enhance the assimilation signal, the observation error was artificially reduced from 1–2 K to 0.5 K. Results are presented in Section 4.1.

As a second step, we carried out two case-studies of three experiments with different control vector settings and control experiments (Table 1) within the fully coupled COSMO-KENDA system (Section 2.2), one two-day early spring case-study in March 2017 and one two-day summer case-study in August 2017. The synthetic case-studies of LST assimilation allowed us to evaluate the performance of the augmented control vector on the whole coupled land–atmosphere system. However, when interpreting the results, it has to kept in mind that they represent only a proof of concept due to the short time periods and the OSSE set-up. For a comprehensive evaluation of the impact, longer experiments with real data have to follow.

The control experiments, *Control*, also known as open loop were run without any assimilation of observations, but also within the hourly assimilation cycle. That means that each hour a new forecast was started from the last first-guess. Within the other experiments, all active LST retrievals were assimilated. The experiments, *EXPatmos*, were performed with the current COSMO-KENDA setting, that is, the control vector included only atmospheric state variables. Therefore, the assimilation of LST had a direct impact on the atmosphere, but only an indirect impact on the soil. The experiments *EXPsoil* included only soil temperature and soil moisture in the control vector. Here, the assimilation of LST had a direct influence on the soil and an indirect influence on the atmosphere. The experiments, *EXPatso*, included soil and atmospheric variables within the control vector, therefore the LST assimilation had a direct effect on the soil and the atmosphere and an indirect effect due to the interaction between the soil and the atmosphere. The impact of LST assimilation on atmospheric and soil temperature was due to background cross-correlations within the LETKF. An overview of the typical correlations during the time period of this study is given in Section 4.1. The observation error was set to values between 1 and 2 K based on the real errors provided by the satellite-derived LST product (Trigo *et al.*, 2008; Freitas *et al.*, 2010; Göttsche *et al.*, 2013). The two-day early spring experiment from 27 to 29 March 2017 started with clear-sky conditions but got cloudier on the second day (Figure 2a), thus on the first day many more LST observations were possible and could be used within the assimilation cycle. The two-day summer experiment from 28 to 30 August 2017, had clear-sky conditions with cloudy sections in the morning (Figure 2b).

4 | RESULTS

4.1 | Coupled system assessment: Single-observation experiments

The SOEs were carried out during the March and August periods to test the functionality of the assimilation of LST in combination with the augmented control vector. Like the boundary layer, LST has a strong diurnal cycle. To see how the effect of LST assimilation varies during the diurnal cycle, the SOEs were performed day and night.

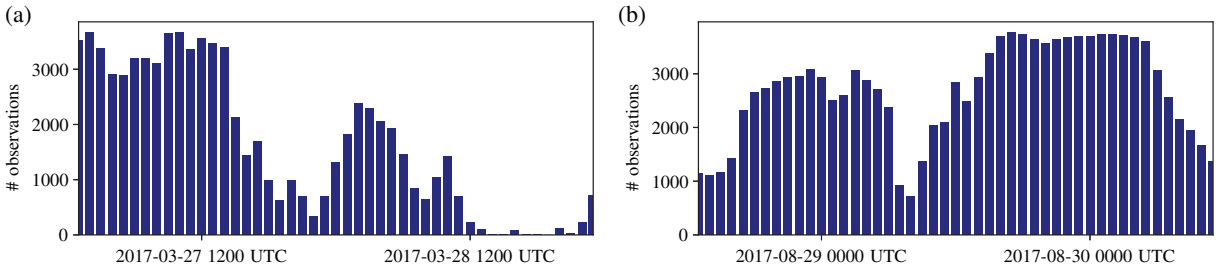

FIGURE 2 Number of active LST retrievals during the two-day experiment periods (a) 27 to 29 March 2017 and (b) 28 to 30 August 2017. Variations are due to cloudiness

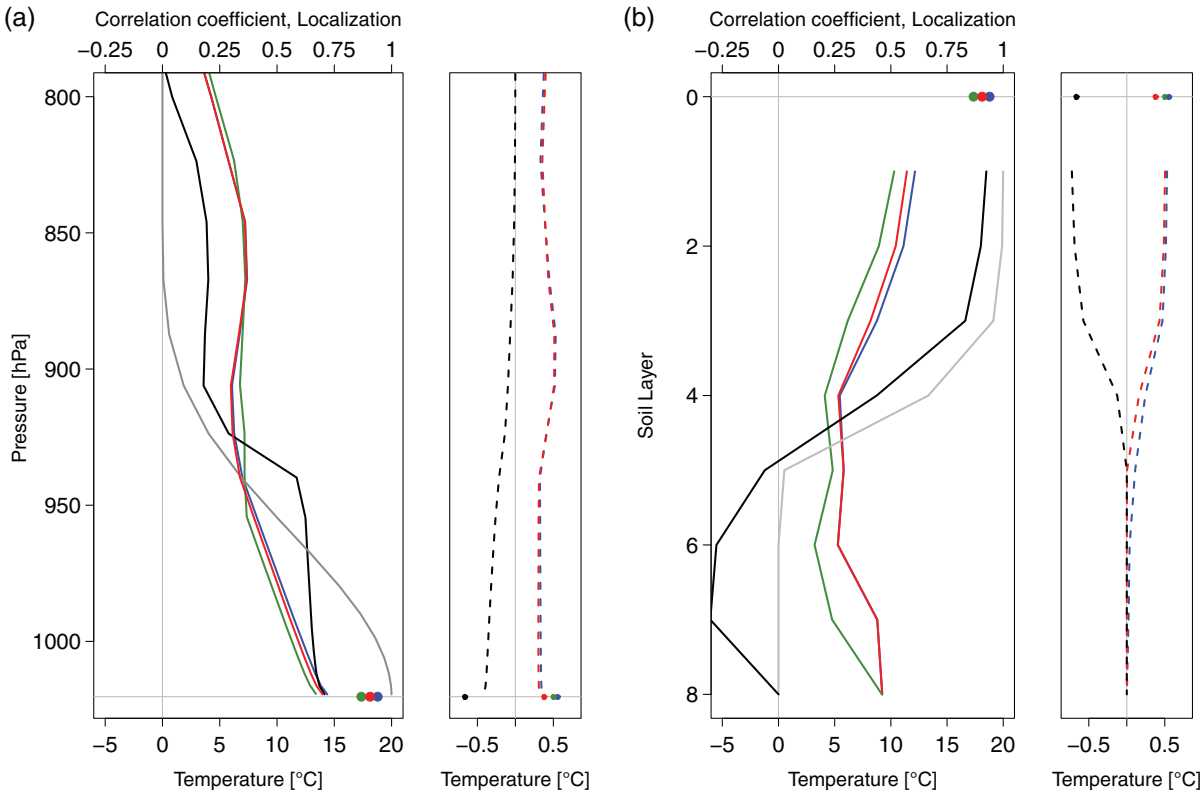

FIGURE 3 **(a)** Impact on atmospheric temperature of LST assimilation at 1400 h on 27 March 2017. Left: profiles of first-guess (blue), analysis (red) and, *truth* (green), localization function (grey), and the correlation between LST and atmospheric temperature (black). The big dots indicate LST first-guess (blue), LST analysis (red) and LST observation (green). Right: atmospheric temperature spread profiles of first-guess (blue, dashed) and analysis (red, dashed) and of the atmospheric temperature increment (black, dashed). The small dots indicate the spreads of LST first-guess (blue), LST analysis (red), LST observation error (green) and LST increment (black). (b) is as (a), but for soil temperature. Location of the SOE: 52.0°N, 14.0°E

4.1.1 | Day: 27 March 2017, 1400 h

As an example, Figure 3 illustrates how the COSMO-KENDA system works for one of the 35 SOEs and how the atmospheric and soil temperature are affected during daytime. Around noon the land surface temperayure is higher than the atmospheric temperature. The synthetic LST observation is colder than the LST model equivalent of the first-guess (Figure 3a). The mixed boundary layer reaches up to 1.5 km and the atmospheric temperature decreases with height up to this level. The atmospheric temperature of the nature run is lower than the atmospheric temperature of the first-guess, but both temperatures decrease with the same gradient. The ABL height of the nature run is lower than the ABL height of the first-guess. The correlation between LST and atmospheric temperature of the first-guess is constant and positive within the ABL. The remaining SOEs have similar covariances within the ABL (not shown). Above the mixed boundary layer, the correlation between LST

and atmospheric temperature differs between the SOEs. The observation error of LST is slightly smaller than the spread of the first-guess model equivalent. The analysis step leads to lower land surface and atmospheric temperatures, which results in a constant, negative increment over the whole ABL. The increment decreases with height as well as the localisation function, which restricts the vertical extension of the LST assimilation impact. Because of the temperature reduction by the analysis step, the atmospheric temperature is closer to the *truth* than the first-guess and the LST analysis is improved as well as the lower atmospheric temperature analysis.

During the day the land surface is warmer than the soil. The soil temperature decreases with depth within the upper soil levels (Figure 3b). The *true* soil temperature has a profile similar to the first-guess temperature, but is lower over all soil layers, except the climate layer, where they are equal, by definition. The first-guess temperature of the upper soil levels and the first-guess LST are positively correlated. All conducted SOEs show this positive correlation decreasing with depth as in the example (Figure 3b). But in the soil levels below 1 m, the correlation is no longer uniform across SOEs. The implemented soil localisation allows an impact of LST assimilation within the layers which are affected by the diurnal cycle. The assimilation of LST shifts the analysis closer to the nature run in the upper soil layers. Therefore, the increment is negative within the five upper soil levels and approaches zero within the deeper levels.

4.1.2 | Night: 27 March 2017, 0200 h

During night the stable stratified boundary layer over northeastern Germany has a height of about 0.5 km. The first-guess and nature run of the SOE have a ground inversion (Figure 4a), that is, the atmospheric temperature increases with height and starts to decrease at the top of the ground inversion at about 0.5 km. The Earth surface is noticeable colder than the air above. For example, the LST model equivalent of the first-guess is almost 10 °C colder than the lowest atmosphere level of the first-guess. The spread of first-guess LST is about 3 °C, thus clearly larger than the observation error of 0.5 °C. The ensemble spread of atmospheric temperature has its maximum near the surface. The localisation equals the localisation of the day (Figure 3), however during night the correlations between first-guess LST and first-guess atmospheric temperature of the 35 SOEs differ (not shown). The LST and the atmospheric temperature of some of the SOEs are correlated, some are anti-correlated, some are not correlated at all and some correlations even lead to wrong increments. Thus the system is working as constructed, but with wrong correlations, wrong increments are produced. In this study, under a high pressure system, the SOEs with anti-correlated behaviour (e.g., Figure 4a) dominate. The correlation within the stable boundary layer is negative and more pronounced close to the land surface. The assimilation of LST pulls the analysis closer to the nature run, hence the increment is negative over the whole ABL. Near the surface the increment values are highest.

During night-time, in contrast to daytime, the upper soil levels are colder than the deeper levels (Figure 4b). The nature run is warmer in the first three levels and colder in the deeper layers than the first-guess. LST and the temperature of the upper soil levels are positively correlated, as during daytime. The increment is positive and decreases with depth as given by the localisation function. The analysis is pulled closer to the nature run, but slightly too strongly, becoming slightly warmer than the nature run.

4.2 | Coupled system assessment: Augmented control vector tests

To examine whether and how the coupled land–atmosphere assimilation system performs, two case-studies in March and August 2017 were conducted. The following results should be seen as a test of concept, as results from OSSEs are generally better than studies based on real observations.

The experiments (Table 1) of the case-studies are evaluated against their respective nature run. The spatial mean error

$$ME = \frac{1}{N}\sum_{i=1}^{N}\{x(i) - x_{\text{true}}(i)\} \tag{15}$$

is calculated to determine systematic deficiencies of simulated boundary-layer and soil temperature. Here N is the number of grid points of the domain excluding the boundary regions, x the temperature of the experiments and x_{true} the temperature of the nature run.

The temporal evolution of the spatial ME of the atmospheric temperature of the two-day spring case is illustrated by Figure 5a. Compared to the nature run, the control run and the experiments have a too high atmospheric temperature within the ABL (Figure 5a). Furthermore, the ME of the control run and the experiments has a diurnal cycle within the ABL, that is, during night and the morning hours the ME is larger than after midday and in the evening. Above the ABL, the ME is negative with values lower than 0.5 K for each experiment. The positive ME of the *Control* has values up to 1.5 K. The three experiments behave similar to the *Control*, however with a reduced ME within the ABL. Especially *EXPatmos* and *EXPatso* have a reduction of spatial ME up to 0.6 K in the morning hours.

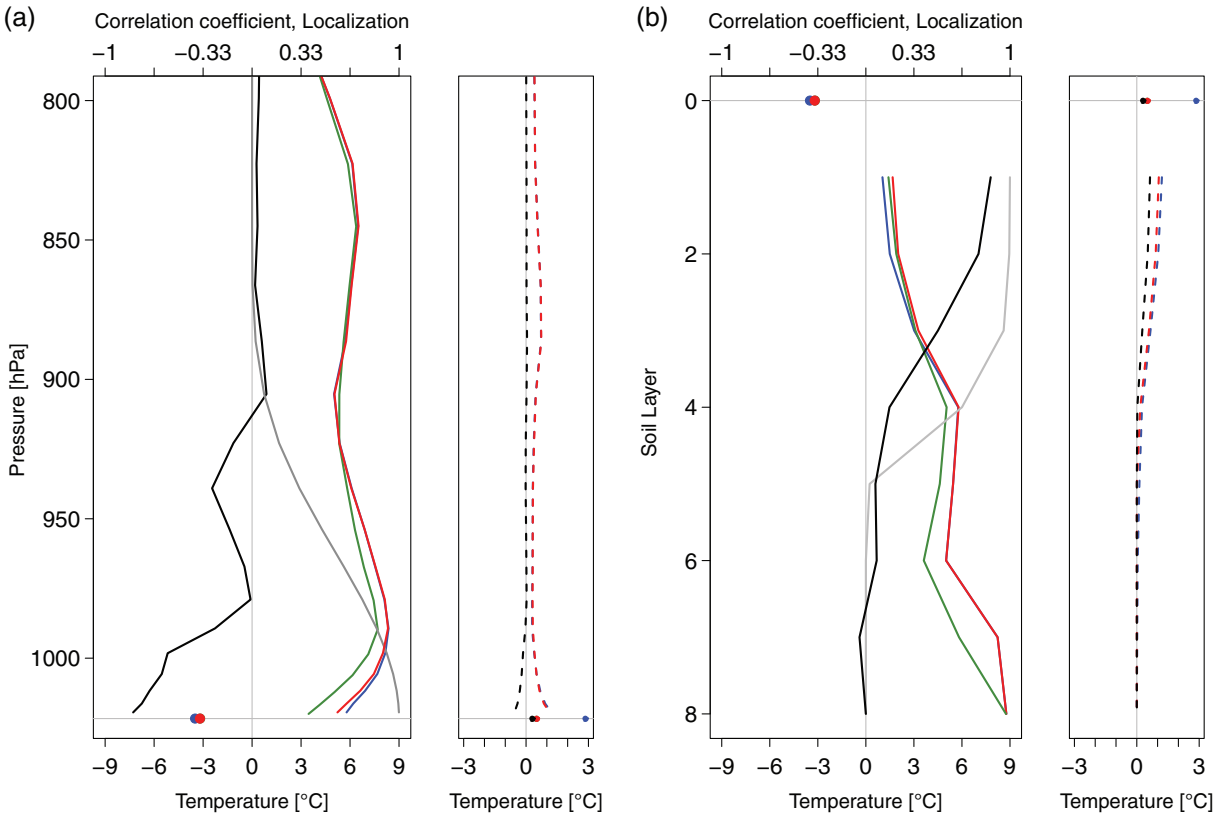

FIGURE 4 As Figure 3, but at 0200 h on 27 March 2017. The synthetic observation of LST (green dot) is located behind the model equivalent LST of the analysis (red dot) and is thus not visible. The same applies to the LST observation error (small green dot), which is located behind the spread of analysis LST (small red dot). Location of the SOE: 53.0°N, 12.5°E

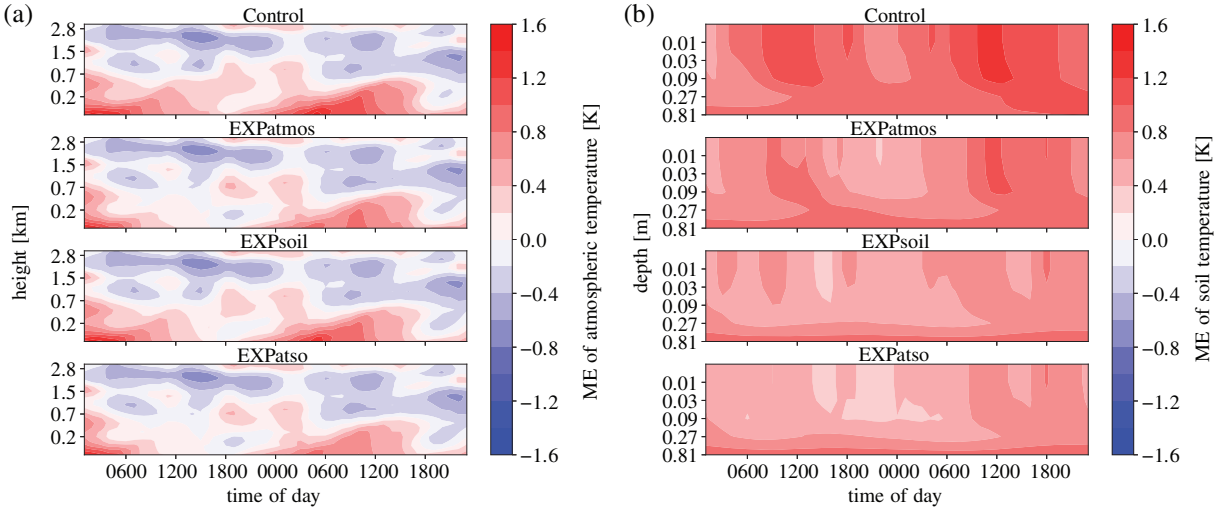

FIGURE 5 Mean error evolution over 27 and 28 March 2017 of temperature for (a) the atmospheric boundary layer and (b) soil levels, for the four experiments. First-guess is evaluated against *truth* averaged over the whole experiment domain. Red shaded areas indicate a warmer model and blue shaded areas indicate a colder model

Above 0.7 km the influence of LST assimilation decreases and the negative ME remains nearly unaffected.

The soil temperature has a consistent positive ME over the upper soil layers and a diurnal cycle (Figure 5b). The diurnal cycle of soil temperature ME has a 6 hr shift compared to the diurnal cycle of the ABL temperature ME, i.e., the ME is highest around midday and lowest around midnight. The *Control* shows this behaviour most clearly. Each

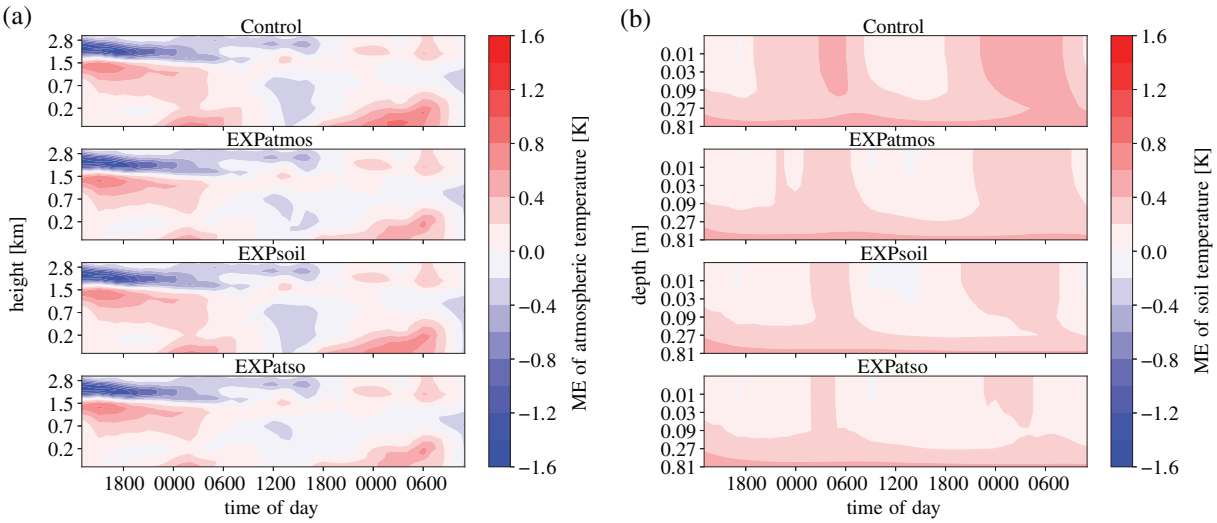

FIGURE 6 As Figure 5, but over 28 to 30 August 2017

of the three spring experiments has a reduced ME compared to *Control*. The ME reduction is most pronounced in *EXPatso* with a reduction of the error of up to 0.7 K around midday.

The temporal evolution of the spatial ME of the atmospheric temperature of the two-day summer case (Figure 6a) has a similar course as the early spring experiments. The atmospheric temperature of the *Control* and the experiments is too high and the ME of the atmospheric temperature also has a diurnal cycle with a maximum ME between 0000 and 0600 UTC. The ME within the ABL of the summer experiments is on average 0.4 K smaller than the ME of the spring experiments, i.e., within the ABL the temperature of the control run and the experiments is closer to the atmospheric temperature of the nature run than in March. From 28 August 1300 UTC to 29 August 0100 UTC, a negative ME is visible between 1.5 and 2.8 km height in each experiment, but as in the spring case the atmospheric temperature above the ABL is nearly unaffected by the assimilation of LST.

The temperature of the upper soil layers of the summer case (Figure 6b) has a consistent positive ME which is on average 0.6 K smaller than the ME of the spring case. The ME is highest between 0000 and 0600 UTC. A reduction of about 0.2 K in ME is visible in all three experiments compared to the ME of the control run.

Next the RMSE

$$RMSE = \sqrt{\frac{1}{N}\sum_{i=1}^{N}\{x(i) - x_{\text{true}}(i)\}^2} \qquad (16)$$

is examined for the boundary layer (Figures 7a and 8a) and soil temperature (Figures 7b and 8b). The RMSE of boundary-layer temperature also has a diurnal cycle, as for the ME. The maximum RMSE within the ABL during the spring and the summer experiments is close to the surface in the lowest 0.1 km between 0000 and 0600 UTC. During the summer experiment another maximum of RMSE is located at the same height as the negative ME (Figure 6a). The RMSE of atmospheric temperature is reduced in each assimilation experiment.

In both the early spring and summer periods, the RMSE of the soil temperature is higher than the RMSE of the boundary-layer temperature. The assimilation of LST reduces the RMSE of each influenced soil level during the summer and spring period, especially if the soil variables are included in the control vector (*EXPsoil* and *EXPatso*). The soil and boundary-layer temperature in the summer case have a smaller RMSE than the early spring case (Figures 7 and 8).

The benefit of the LST assimilation relative to the *Control* is estimated by the relative change of RMSE (rRMSE, %):

$$rRMSE = \frac{RMSE - RMSE_{\text{Control}}}{RMSE_{\text{Control}}} \times 100\,, \qquad (17)$$

where $RMSE$ is the RMSE of the respective experiment and $RMSE_{\text{Control}}$ is the RMSE of the open loop (*Control*).

During the two-day spring period, the RMSE of boundary-layer temperature is reduced in all three experiments (Figure 9a), during daytime up to 60% near the ground. The main improvement of RMSE of *EXPatmos* is between 0600 and 1200 UTC on 27 March (Figure 9a, top).

The reduction of RMSE of *EXPsoil* is shifted compared to *EXPatmos* by approximately 6 hr through the indirect effect of the improved soil state and has its maximum during the afternoon (Figure 9a, middle). *EXPatso* successfully combines both improvements but also includes

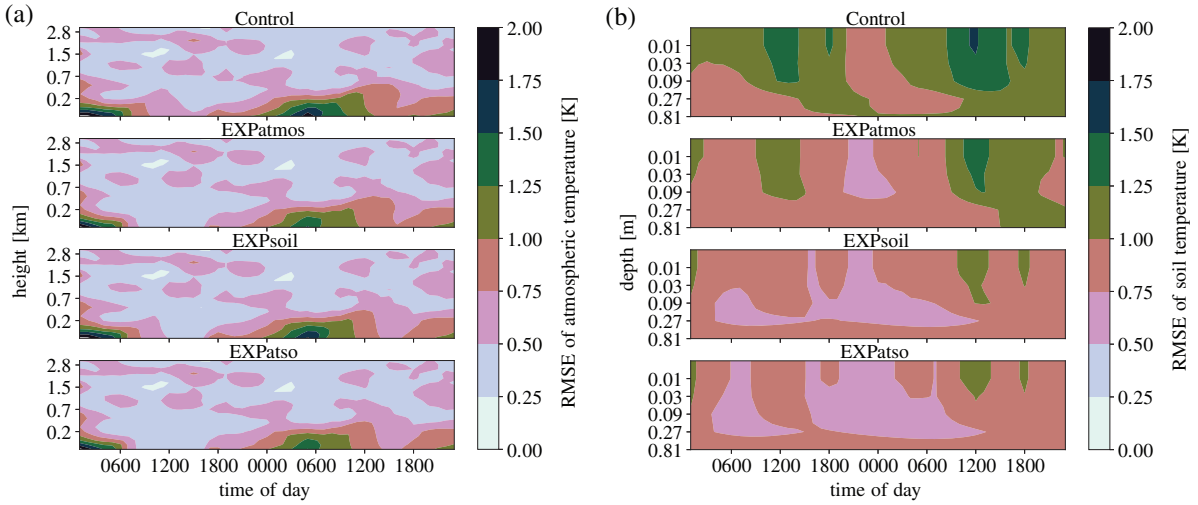

FIGURE 7 RMSE evolution over 27 and 28 March 2017 of temperature for (a) the atmospheric boundary layer and (b) soil levels, for the four experiments. First-guess is evaluated against *truth* averaged over the whole experiment domain. Darker areas indicate larger RMSE

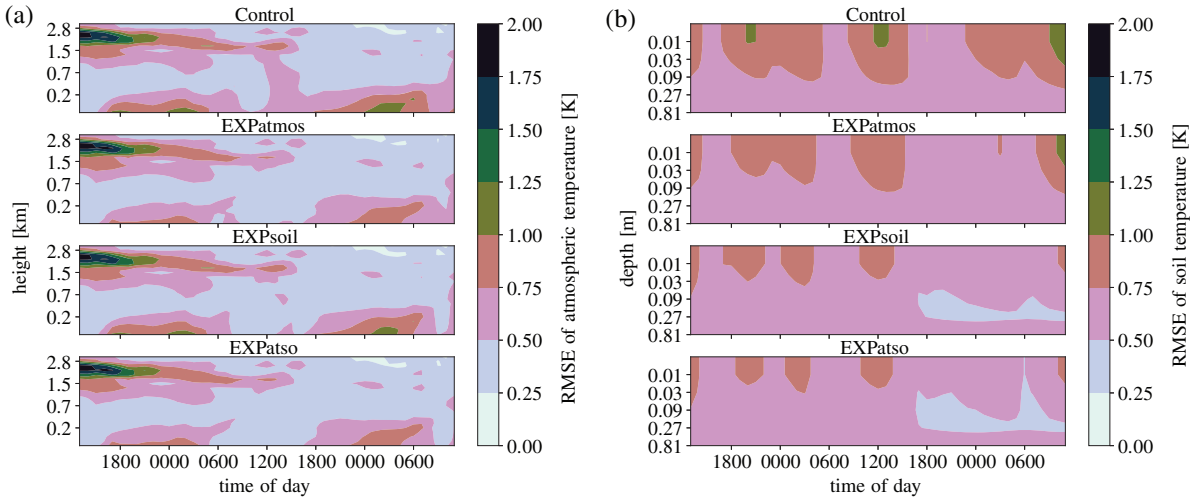

FIGURE 8 As Figure 7, but over 28 to 30 August 2017

the increased RMSE of *EXPatmos* at the top of the ABL (Figure 9a, bottom).

The RMSE of the soil temperature is also reduced by the assimilation of LST, partly up to 50% (Figure 9b). The effect is best if the coupled assimilation setting is performed (*EXPatso*). The deeper soil layers keep the positive effect over a longer period than the upper soil levels.

All in all, the effect of LST assimilation during the two days of March is stronger during the first day because more LST observations were available and could be assimilated. On the second day, a cloud pattern over northeastern Germany reduced the number of observations, and, consequently, the available LST information within the assimilation cycle (Figure 2a).

During the two-day summer period, the RMSE of boundary-layer temperature is reduced in all three experiments. As in the two-day case in March, the main reduction is during daytime, but with its maximum up to 40% in the afternoon (Figure 10a). In the afternoon of 29 August, the positive effect of LST assimilation on the atmospheric temperature reaches up to a height of 1.5 km within the experiments including the atmosphere in their control vector (*EXPatmos* and *EXPatso*; Figure 10a, top and bottom). During the night from 29 to 30 August, *EXPatmos* and *EXPatso* show an increase of the RMSE of the atmospheric temperature located above the ABL. A different vertical localisation during night and day could be an option to avoid this effect. The impact of LST assimilation on the RMSE of atmospheric temperature of *EXPsoil* is seen during daytime up to a height of 0.7 km and does not lead to an increase of RMSE (Figure 10a, middle).

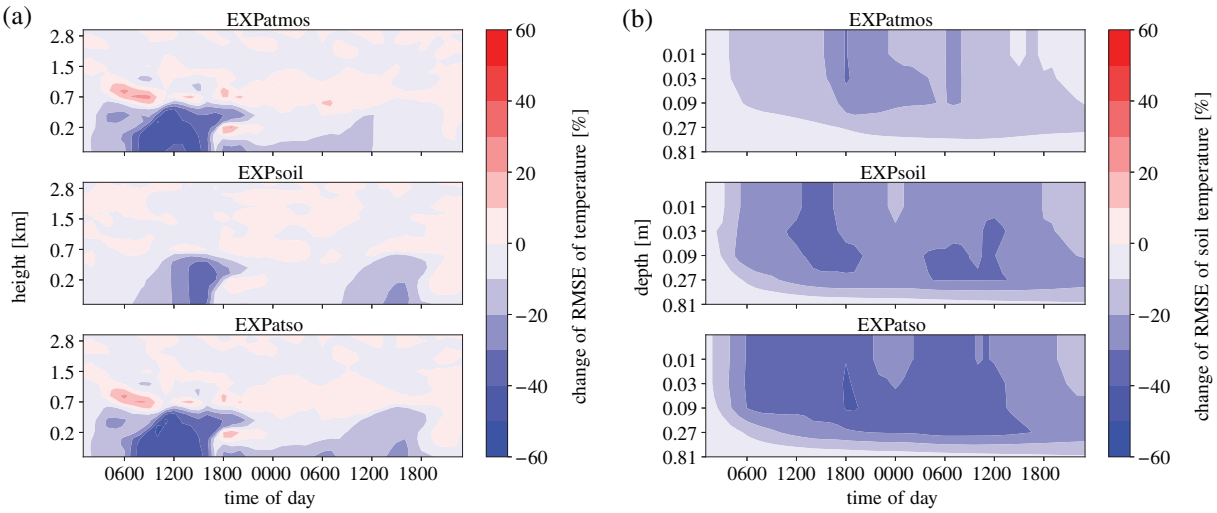

FIGURE 9 Change against *Control* in rRMSE evolution over 27 and 28 March 2017 of temperature for (a) the atmospheric boundary layer and (b) soil levels, for the three experiments. First-guess is evaluated against *truth* averaged over the whole experiment domain. Blue shading indicates an improved RMSE within the assimilation experiment against *Control*, and red shading indicates a deterioration

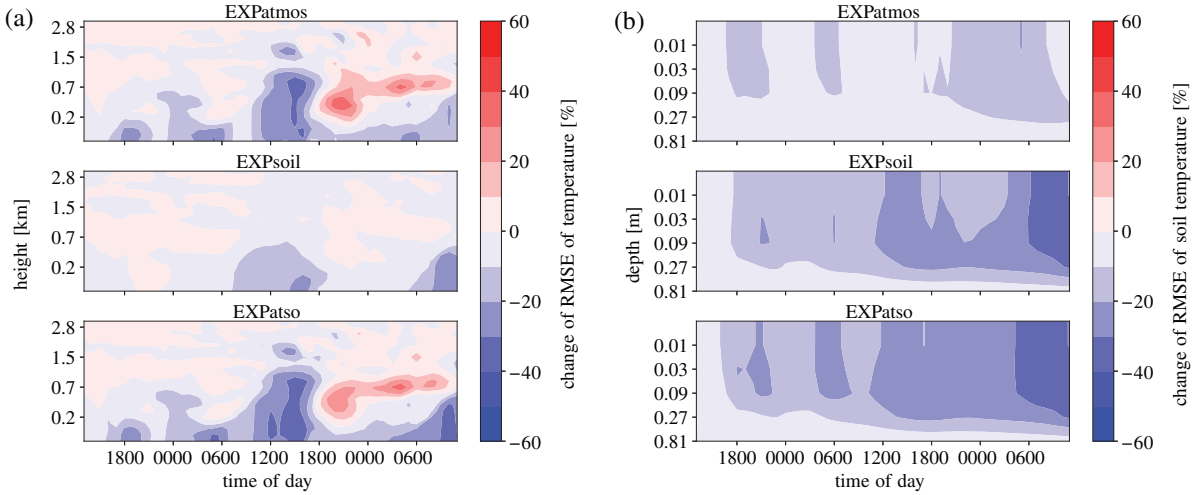

FIGURE 10 As Figure 9, but over 28 to 30 August 2017

The RMSE of the soil temperature is consistently reduced in each summer experiment. The RMSE decreases as the number of assimilated synthetic LST observations increases (Figures 2b and 10b). As in the spring period, the deeper soil layers keep the positive effect longer than the upper soil layers.

4.2.1 | Impact on atmospheric humidity and soil moisture

Besides temperature, moisture variables in the ABL and the soil are also influenced by the LST assimilation through cross-correlations. The direct effect of LST assimilation in *EXPatmos* and *EXPatso* reduces the atmospheric specific humidity clearly too much (Figure 11a, top and bottom). The RMSE of specific humidity within this two experiments reaches up to 70%. This remarkable increase takes mainly place in the morning transition. The negative influence of LST assimilation can be due to inappropriate covariances. In contrast, the specific humidity of *EXPsoil* benefits from the assimilation of LST. On the afternoon of the second day of the experimental period, the RMSE of relative humidity is reduced by more than 10% (Figure 11a, middle). Because fewer LST observations are assimilated during this period, we assume that the improvement is due to the accumulated effects of an improved state of the soil. This positive effect is even more evident in *EXPatso*.

In contrast to the atmospheric humidity, the soil moisture can benefit from the direct effect of LST

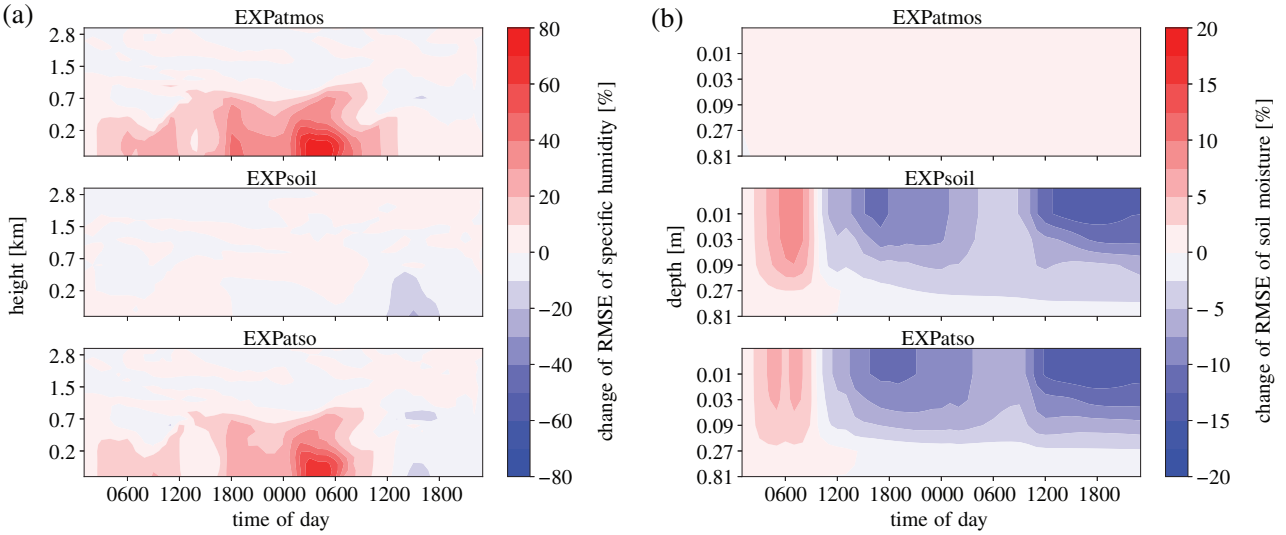

FIGURE 11 Change against *Control* in rRMSE evolution over 27 and 28 March 2017 of (a) specific humidity of the atmospheric boundary layer and (b) soil moisture, for the three experiments. Details are as Figure 9

assimilation within the soil in March by introducing moisture (Figure 11b). Within the first 6 hr the assimilation of LST dries the soil, but after 12 hr of LST assimilation moisture is introduced into the soil by LST assimilation, which reduces the RMSE mainly during daytime by more than 12%. But this positive impact only occurs if the soil temperature and moisture are part of the control vector (Figure 11b, middle and bottom). In the case where only the atmospheric variables are part of the control vector, the assimilation of LST has hardly any impact on the soil moisture. The RMSE of *EXPatmos* is slightly increased (by less than 2.5%), but mostly it is close to the *Control* (Figure 11b, top).

As in the early spring case, the RMSE of specific humidity of *EXPatmos* and *EXPatso* in the summer case increases during the morning transition, but only on the first day (Figure 12a, top and bottom). On the second day, the RMSE of specific humidity increases during the night and morning transition (Figure 12a, middle and bottom).

The difference between the soil moisture down to 0.5 m in the nature run and the assimilation experiments is smaller for the summer cases. The soil of the assimilation experiments is only about 5% drier than the nature run (not shown). The deeper layers of the assimilation experiments are more moist than the nature run, however they were unaffected by the LST assimilation. As in the spring case, the assimilation of LST introduces moisture into the upper soil levels after 12 hr of assimilation (Figure 12b, middle and bottom). The upper soil levels become too moist and only the deeper layers benefit from the additional moisture. As in spring, the RMSE of *EXPatmos* is nearly unaffected (Figure 12b, top).

4.2.2 | Evaluation of 24 hr forecasts

The assimilation of LST led to improved initial conditions for the ABL and the soil of the forecast model. To investigate the effect of LST assimilation on the COSMO model forecast, a 24 hr forecast was simulated every 6 hr. The free forecasts were initialised from *Control* and *EXPatso* for the two-day experiments in March and August.

As illustrated in Figure 13a, the LST assimilation during the two-day study in March 2017 based on *EXPatso* has a positive impact on the temperature of the ABL. In the *EXPatso* forecast started at 0600 UTC, the RMSE is reduced by over 20% in the first ten forecast hours within the lower levels of the atmosphere up to 0.7 km (Figure 13a, top). In contrast, at the top of the ABL, the first three forecast hours have an increased RMSE by about 10 to 20%. After twelve forecast hours the reduction of RMSE is negligible.

The forecast started on 27 March at 1200 UTC has also an improved ABL temperature because of LST assimilation (Figure 13a, middle). The positive effect on ABL temperature lasts for 4 hr near to the surface and for 6 hr between 0.2 to 0.7 km. After six to nine hours of forecast, around the evening transition, the ABL temperature RMSE is 10% larger than of *Control*. This negative effect is reduced to around 3% after 9 hr of forecast. The forecast started on 27 March at 1800 UTC shows only short-lived improvements of LST assimilation (Figure 13a, bottom). Because of the growing cloud cover, fewer LST observations were available, which results in a smaller impact of LST assimilation. Around 18 hr of forecast a RMSE reduction of 15% occurs, possibly due to the indirect effect of improved soil variables.

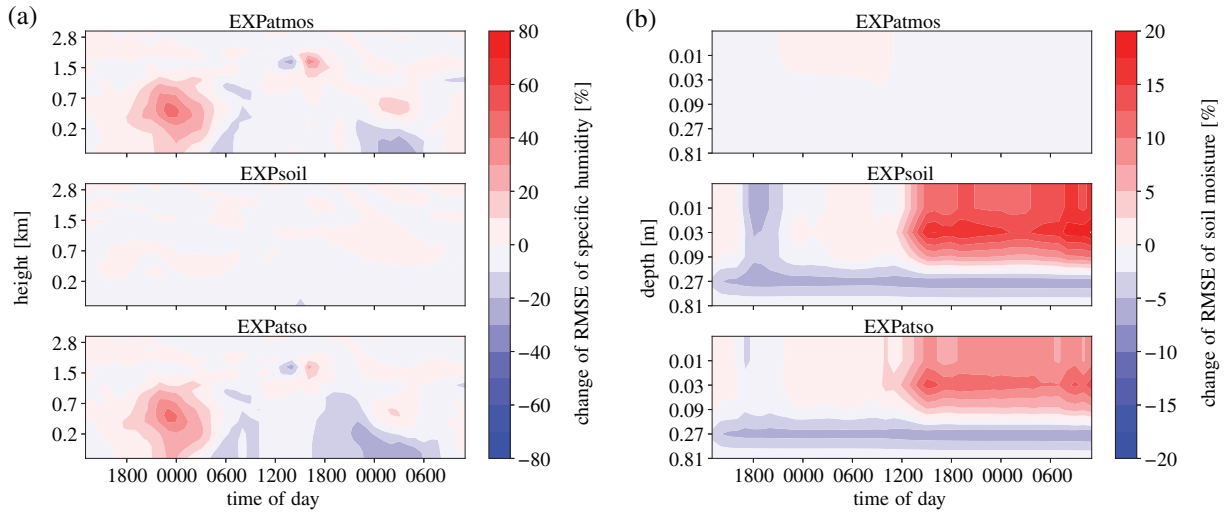

FIGURE 12 As Figure 11, but over 28 to 30 August 2017

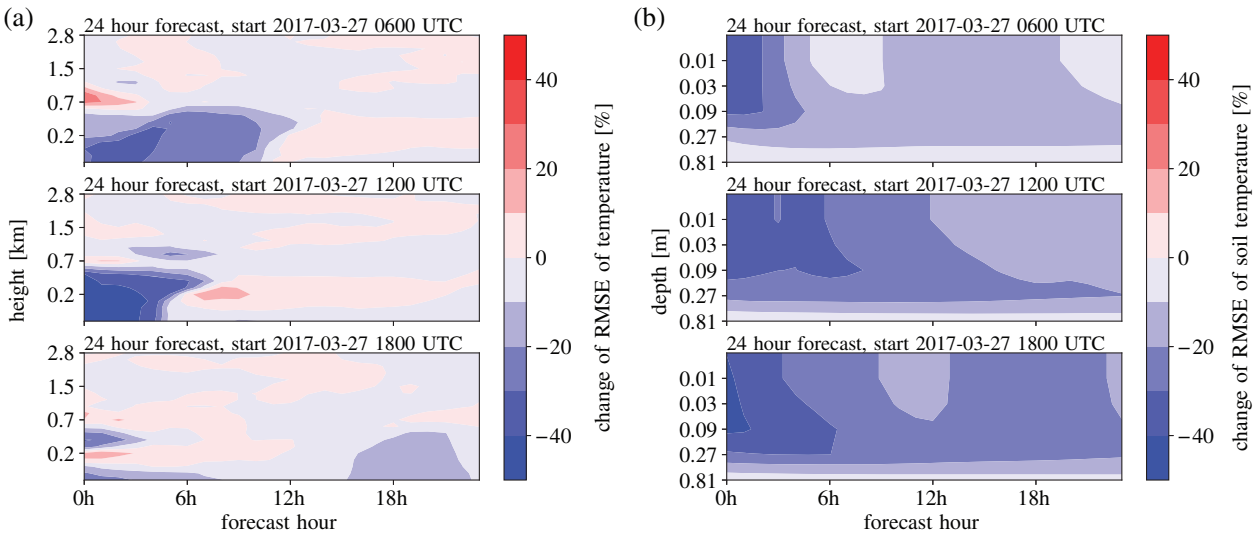

FIGURE 13 Change of rRMSE (*EXPatso* against *Control*) for the early spring case for three free 24 hr forecasts of temperature of (a) the atmospheric boundary layer and (b) soil levels, started after 6 hr (top), 12 hr (middle) and 18 hr (bottom) of LST assimilation. The forecasts started from *EXPatso* and the *Control* are evaluated against the *truth* averaged over the whole experiment domain. Blue shading indicates an improved RMSE within *EXPatso*, and red shading indicates a deterioration

In general, the soil temperature forecast is improved by the LST assimilation over each soil level down to 1 m (Figure 13b). The soil temperature RMSE of the forecast started at 0600 UTC is mainly reduced during the first three forecast hours within the upper 0.1 m of the soil. The forecast started at 1200 UTC includes an even bigger reduction of soil temperature RMSE up to 6 hr down to 0.5 m. A reduction of soil temperature RMSE around 20% lasts for the whole 24 hr forecast, that is, the soil temperature keeps the effect of LST assimilation longer than the ABL temperature. The reduction of soil temperature RMSE over 20% remains over the whole 24 hr of the forecast started at 1800 UTC.

The 24 hr forecasts of atmospheric temperature and soil temperature based on *EXPatso* of the two-day study in August 2017 also benefit from the LST assimilation (Figure 14a), but the benefit is less pronounced than during the two-day study in March 2017. The first four forecast hours of the temperature of the ABL started at 0000 UTC have a 10% reduced RMSE and a further reduction of more than 10% around 12 hr of forecast (Figure 14a, top).

In the *EXPatso* forecast started at 0600 UTC, the RMSE of the atmospheric temperature is reduced over the first 12 hr (Figure 14a, middle). The reduction of the RMSE up to the height of 0.2 km ranges between 10 and 30% (only the first forecast hour).

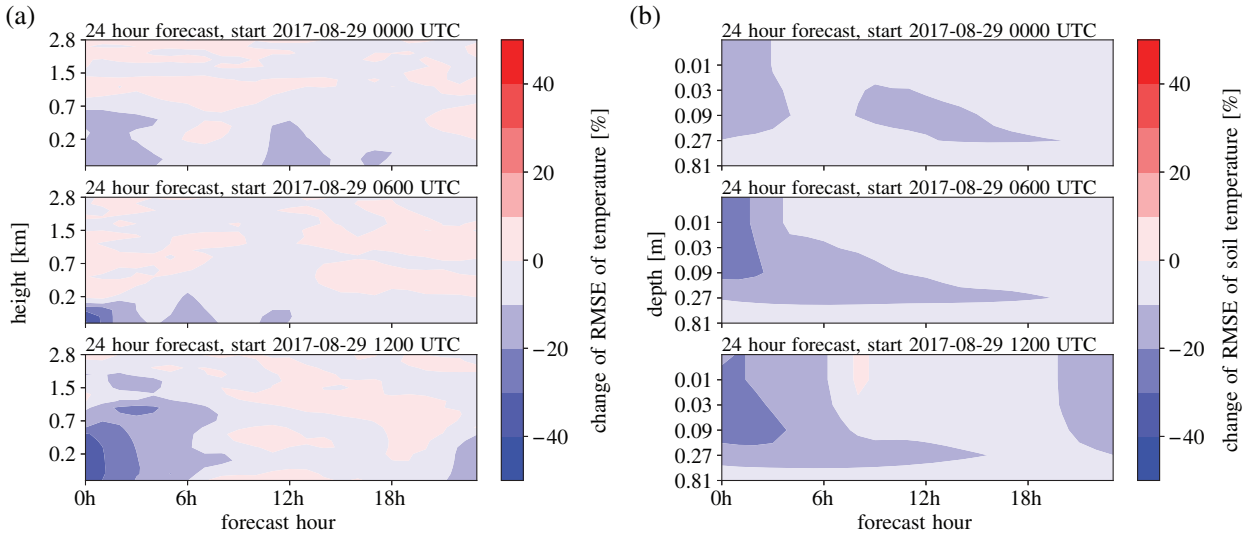

FIGURE 14 As Figure 13, but for the summer case

The forecast started on 29 August at 1200 UTC profits from the LST assimilation during the first six forecast hours. The forecast of the atmospheric temperature is improved up to a height of 1.5 km (Figure 14a bottom). After 22 hr a RMSE reduction of 15% arises. This reduction coincides with an improvement of soil temperature of the same forecast which indicates that the soil may have a positive effect on the atmosphere over the whole 24 hr forecast.

As in March, the soil temperature forecast is also improved in August. The assimilation of LST reduces the RMSE of the forecast of the soil temperature down to 1 m, with the main reduction occurring in the first three forecast hours (Figure 14b. The forecasts started at 0600 and 1200 UTC keep the reduction of the RMSE of soil temperature longer than the forecast started 0000 UTC, especially in the deeper layers between 0.1 and 0.3 m (Figure 14b middle and bottom). After 20 forecast hours from the forecast started at 1200 UTC, the reduction of RMSE of soil temperature increases again (Figure 14b bottom).

To summarize, the soil temperature, especially the levels between 0.1 to 0.3 m, keep the positive impact of LST assimilation longer than the ABL temperature. The soil moisture also keeps the positive or negative impact longer than the specific humidity of the ABL (not shown).

5 | DISCUSSION AND CONCLUSION

LST has been assimilated in an OSSE framework in a coupled land–atmosphere NWP model. It is the first time that LST has been assimilated simultaneously for the land and the atmosphere within the fully coupled land–atmosphere data assimilation system COSMO-KENDA. By this assimilation approach we go further than Candy *et al.* (2017) and Bosilovich *et al.* (2007), who assimilated LST into a land model, which was coupled with an atmospheric model. Our experiments show that, in the LETKF framework, a simultaneous assimilation outperforms a assimilation of LST restricted to land or atmosphere only. The positive impact of LST assimilation on the first-guess was larger during daytime, where a stronger coupling between LST and ABL temperature was found.

The impact of synthetic LST assimilation on the atmosphere and the soil was due to the background cross-correlations of the LETKF. The correlation between surface and atmospheric temperature depends on the time of day (Figures 3a and 4a). During the day, the LST and the temperature of the ABL were positively correlated because of the well-mixed boundary layer. The correlation between LST and ABL temperature realistically represents the interaction between the land and the atmosphere due to turbulent fluxes. During the night, the correlation between LST and the temperature of the ABL was less clear, which could be the result of the poorer representation of the stable boundary layer (Holtslag *et al.*, 2013). Furthermore, the energy exchange by turbulent fluxes between the land and the atmosphere is weaker within the stable boundary layer than within the mixed boundary layer. The weaker interaction between the land and the atmosphere is represented by lower correlations between LST and ABL temperature during the night. The correlation between LST and soil temperature of the upper levels was always positive, hence the soil temperature follows LST over the whole diurnal cycle. In contrast, the deeper soil layers do not change considerably within a day and were more or less uncorrelated with LST.

The two-day experiments of March and August 2017 confirm the SOEs and provide insight into the direct and indirect impact of LST assimilation within the coupled assimilation system. The direct effect of LST assimilation on the atmosphere (Figures 9a and 10a, top) depends on the diurnal cycle and the amount of available LST retrievals. The improvement due to LST assimilation seems to increase with the growth of the mixed boundary layer and to decrease with the transition to the nocturnal stable boundary layer. Above the ABL and during the evening transition, LST assimilation had a negative impact. This could be a sign of wrong ensemble correlations. A stricter vertical localization, in particular during the night, could reduce the negative impact. The effects on humidity/moisture variables was mixed in this study. The assimilation of LST had a positive impact on atmospheric humidity in the afternoon and a negative impact during the morning transition (Figures 11a and 12a). The soil moisture can improve if additional moisture is introduced at an appropriate time (Figures 11b and 12b). This could be improved further by the combined assimilation of LST and moisture observations. Synthetic studies by Han *et al.* (2013) (joint assimilation of LST and microwave brightness temperature) and Abdolghafoorian and Farhadi (2019) (joint assimilation of soil moisture and LST) and the study with real data (joint assimilation of LST and reference-level temperature and relative humidity) by Tajfar *et al.* (2020b) showed promising steps in this direction. The number of LST retrievals and the direct effect of LST assimilation were both smaller on the second day, indicating that the information of LST assimilation does not last long in the atmosphere. In contrast, the information of LST assimilation in the atmosphere has a longer-lasting positive indirect impact on the soil which shifts to deeper levels (Figure 9b, top). The direct impact of LST assimilation in the soil was even stronger and also reduced the RMSE of the soil temperature during the whole period (Figure 9b, middle). The effect is reduced if less LST information is available, but the longer memory of the soil keeps the information better than the atmosphere. Therefore, the indirect impact of the soil on the atmosphere is crucial because it can improve the simulated atmospheric temperature even if less new LST information is available (Figure 9a, middle). To conclude, the combination of a strong direct impact on the atmosphere and longer-lasting indirect impact by the soil is promising and was able to reduce near-surface atmospheric temperature RMSE up to 60% and the temperature of the upper soil levels up to 40% (Figure 9, bottom). The better representation of ABL temperature may potentially improve forecasts of ABL processes like convection, clouds, moist convection, and fog formation.

The direct improvement of LST assimilation in the ABL depends strongly on the available retrievals at the initial time of the forecast, because the atmosphere is not able to keep the information over a long time period. If the LST retrieval is exhaustively available, the forecast of the atmospheric temperature can be improved by up to 6 hr by the direct effect (Figures 13a and 14a). Because the soil temperature varies on longer time-scales than the atmospheric temperature, the soil keeps the information of LST assimilation during the whole forecast and its state improves further if LST is assimilated more often (Figures 13b and 14b). Through the coupling between the soil and the atmosphere, this also has an indirect positive impact on the forecast of the atmospheric temperature even after 15 to 24 forecast hours (Figures 13a, bottom and 14a).

Our work is restricted to the set-up of an OSSE and an equal benefit of LST assimilation for operational systems with real data is not guaranteed. However, the results encourage the evaluation of LST assimilation within the coupled system with real LST retrievals.

In future studies, as well as the diurnal cycle, the annual cycle also has to be explored and longer experiment periods have to be conducted. Furthermore the experiment domain should be extended. For example, Candy *et al.* (2017) found a benefit to forecasts of near-surface temperature due to LST assimilation, particularly over Africa.

ACKNOWLEDGEMENTS

This research was carried out as part of the Hans Ertel Centre for Weather Research. This German research network of Universities, Research Institutes and the Deutscher Wetterdienst is funded by the BMVI (Federal Ministry of Transport and digital Infrastructure). We thank Dr Jan-Peter Schulz for assistance with the implementation of the skin conductivity scheme. We thank two anonymus reviewers for their critical reading and their valuable suggestions to improve the manuscript. Open access funding enabled and organized by Projekt DEAL.

ORCID

Christine Sgoff https://orcid.org/0000-0003-3541-023X

REFERENCES

Abdolghafoorian, A. and Farhadi, L. (2019) Estimation of surface turbulent fluxes from land surface moisture and temperature via a variational data assimilation framework. *Water Resources Research*, 55(6), 4648–4667. https://doi.org/10.1029/2018WR024580

Aires, F., Prigent, C. and Rossow, W.B. (2004) Temporal interpolation of global surface skin temperature diurnal cycle over land under clear and cloudy conditions. *Journal of Geophysical Research: Atmospheres*, 109(D4). https://doi.org/10.1029/2003JD003527

Baldauf, M., Förstner, J., Klink, S., Reinhardt, T., Schraff, C., Seifert, A. and Stephan, K. (2011a). Kurze Beschreibung

des Lokal-Modells Kürzestfrist COSMO-DE (LMK) und seiner Datenbank auf dem Datenserver des DWD. Technical Report, Geschäftsbereich Forschung und Entwicklung, Deutscher Wetterdienst, Offenbach, Germany.

Baldauf, M., Seifert, A., Förstner, J., Majewski, D., Raschendorfer, M. and Reinhardt, T. (2011b) Operational convective-scale numerical weather prediction with the COSMO model: description and sensitivities. *Monthly Weather Review*, 139(12), 3887–3905. https://doi.org/10.1175/MWR-D-10-05013.1

Bateni, S.M., Entekhabi, D. and Castelli, F. (2013a) Mapping evaporation and estimation of surface control of evaporation using remotely sensed land surface temperature from a constellation of satellites. *Water Resources Research*, 49(2), 950–968. https://doi.org/10.1002/wrcr.20071

Bateni, S.M., Entekhabi, D. and Jeng, D.-S. (2013b) Variational assimilation of land surface temperature and the estimation of surface energy balance components. *Journal of Hydrology*, 481, 143–156. https://doi.org/10.1016/j.jhydrol.2012.12.039

Blahak, U. (2015) Implementation and significance of TKE-advection in COSMO 5.0 for itype_turb=3 and other turbulence-related LES-like sensitivity studies including 3D turbulence. *COSMO Newsletter*, 15, 11–20

Bosilovich, M.G., Radakovich, J.D., da Silva, A., Todling, R. and Verter, F. (2007) Skin temperature analysis and bias correction in a coupled land–atmosphere data assimilation system. *Journal of the Meteorological Society of Japan. Series II*, 85A, 205–228. https://doi.org/10.2151/jmsj.85A.205

Bosveld, F.C., Baas, P., Steeneveld, G.-J., Holtslag, A.A.M., Angevine, W.M., Bazile, E., de Bruijn, E.I.F., Deacu, D., Edwards, J.M., Ek, M., Larson, V.E., Pleim, J.E., Raschendorfer, M. and Svensson, G. (2014) The third GABLS intercomparison case for evaluation studies of boundary-layer models. Part B: results and process understanding. *Boundary-Layer Meteorology*, 152(2), 157–187. https://doi.org/10.1007/s10546-014-9919-1. ISSN 1573-1472)

Candy, B., Saunders, R.W., Ghent, D. and Bulgin, C.E. (2017) The impact of satellite-derived land surface temperatures on numerical weather prediction analyses and forecasts. *Journal of Geophysical Research: Atmospheres*, 122(18), 9783–9802. https://doi.org/10.1002/2016JD026417

Doms, G., Förstner, J., Heise, E., Herzog, H.-J., Mironov, D., Raschendorfer, M., Reinhardt, T., Ritter, B., Schrodin, R., Schulz, J.-P. and Vogel, G. (2011). A description of the nonhydrostatic regional COSMO model. Part II: physical parameterization. Technical Report, Deutscher Wetterdienst, Offenbach, Germany.

Evensen, G. (1994) Sequential data assimilation with a nonlinear quasi-geostrophic model using Monte Carlo methods to forecast error statistics. *Journal of Geophysical Research: Oceans*, 99(C5), 10143–10162. https://doi.org/10.1029/94JC00572

Freitas, S.C., Trigo, I.F., Bioucas-Dias, J.M. and Goettsche, F.-M. (2010) Quantifying the uncertainty of land surface temperature retrievals from SEVIRI/Meteosat. *IEEE Transactions on Geoscience and Remote Sensing*, 48(1–2), 523–534. https://doi.org/10.1109/TGRS.2009.2027697

Gaspari, G. and Cohn, S.E. (1999) Construction of correlation functions in two and three dimensions. *Quarterly Journal of the Royal Meteorological Society*, 125, 723–757. https://doi.org/10.1002/qj.49712555417

Ghent, D., Kaduk, J., Remedios, J., Ardö, J. and Balzter, H. (2010) Assimilation of land surface temperature into the land surface model JULES with an ensemble Kalman filter. *Journal of Geophysical Research: Atmospheres*, 115(D19). https://doi.org/10.1029/2010JD014392

Göttsche, F.-M., Olesen, F.-S. and Bork-Unkelbach, A. (2013) Validation of land surface temperature derived from MSG/SEVIRI with *in situ* measurements at Gobabeb, Namibia. *International Journal of Remote Sensing*, 34(9–10), 3069–3083. https://doi.org/10.1080/01431161.2012.716539

Han, X., Hendricks Franssen, H.-J., Li, X., Zhang, Y., Montzka, C. and Vereecken, H. (2013) Joint assimilation of surface temperature and L-band microwave brightness temperature in land data assimilation. *Vadose Zone Journal*, 12(3). https://doi.org/10.2136/vzj2012.0072

Holtslag, A.A.M., Steeneveld, G.J. and van de Wiel, B.J.H. (2007). Role of land-surface temperature feedback on model performance for the stable boundary layer, pp. 205–220 in *Atmospheric Boundary Layers: Nature, theory and applications to environmental modelling and security*, DOI 10.1007/978-0-387-74321-9_14, (to appear in print). Baklanov, A., Grisogono, B. (eds). Springer, New York, NY.

Holtslag, A.A.M., Svensson, G., Baas, P., Basu, S., Beare, B., Beljaars, A.C.M., Bosveld, F.C., Cuxart, J., Lindvall, J., Steeneveld, G.J., Tjernström, M. and Van De Wiel, B.J.H. (2013) Stable atmospheric boundary layers and diurnal cycles: challenges for weather and climate models. *Bulletin of the American Meteorological Society*, 94(11), 1691–1706. https://doi.org/10.1175/BAMS-D-11-00187.1

Huang, C., Li, X., Lu, L. and Gu, J. (2008) Experiments of one-dimensional soil moisture assimilation system based on ensemble Kalman filter. *Remote Sensing of Environment*, 112(3), 888–900. https://doi.org/10.1016/j.rse.2007.06.026

Hunt, B.R., Kostelich, E.J. and Szunyogh, I. (2007) Efficient data assimilation for spatiotemporal chaos: a local ensemble transform Kalman filter. *Physica D: Nonlinear Phenomena*, 230(1–2), 112–126. https://doi.org/10.1016/j.physd.2006.11.008

Jin, M. (2004) Analysis of land skin temperature using AVHRR observations. *Bulletin of the American Meteorological Society*, 85(4), 587–600. https://doi.org/10.1175/BAMS-85-4-587

Koster, R.D., Sud, Y.C., Guo, Z., Dirmeyer, P.A., Bonan, G., Oleson, K.W., Chan, E., Verseghy, D., Cox, P., Davies, H., Kowalczyk, E., Gordon, C.T., Kanae, S., Lawrence, D., Liu, P., Mocko, D., Lu, C.-H., Mitchell, K., Malyshev, S., McAvaney, B., Oki, T., Yamada, T., Pitman, A., Taylor, C.M., Vasic, R. and Xue, Y. (2006) GLACE: the global land–atmosphere coupling experiment. Part I: overview. *Journal of Hydrometeorology*, 7(4), 590–610. https://doi.org/10.1175/JHM510.1

Margulis, S.A. and Entekhabi, D. (2003) Variational assimilation of radiometric surface temperature and reference-level micrometeorology into a model of the atmospheric boundary layer and land surface. *Monthly Weather Review*, 131(7), 1272–1288. https://doi.org/10.1175/1520-0493(2003)131<1272:VAORST>2.0.CO;2

McNider, R.T., Song, A.J., Casey, D.M., Wetzel, P.J., Crosson, W.L. and Rabin, R.M. (1994) Toward a dynamic–thermodynamic assimilation of satellite surface temperature in numerical atmospheric models. *Monthly Weather Review*, 122(12), 2784–2803. https://doi.org/10.1175/1520-0493(1994)122<2784:TADTAO>2.0.CO;2

Noilhan, J. and Planton, S. (1989) A simple parameterization of land surface processes for meteorological models. *Monthly*

Weather Review, 117(3), 536–549. https://doi.org/10.1175/1520-0493(1989)117<0536:ASPOLS>2.0.CO;2

Pinjosovsky, H.S.B., Thiria, S., Ottlé, C., Brajard, J., Badran, F. and Maugis, P. (2017) Variational assimilation of land surface temperature within the ORCHIDEE land surface model version 1.2.6. *Geoscientific Model Development*, 10(1), 85–104. https://doi.org/10.5194/gmd-10-85-2017

Reichle, R.H., Kumar, S.V., Mahanama, S.P.P., Koster, R.D. and Liu, Q. (2010) Assimilation of satellite-derived skin temperature observations into land surface models. *Journal of Hydrometeorology*, 11(5), 1103–1122. https://doi.org/10.1175/2010JHM1262.1

Ritter, B. and Geleyn, J.-F. (1992) A comprehensive radiation scheme for numerical weather prediction models with potential applications in climate simulations. *Monthly Weather Review*, 120(2), 303–325. https://doi.org/10.1175/1520-0493(1992)120<0303:ACRSFN>2.0.CO;2

Sandu, I., Beljaars, A., Bechtold, P., Mauritsen, T. and Balsamo, G. (2013) Why is it so difficult to represent stably stratified conditions in numerical weather prediction (NWP) models?. *Journal of Advances in Modeling Earth Systems*, 5(2), 117–133. https://doi.org/10.1002/jame.20013

Santanello, J.A., Kumar, S.V., Peters-Lidard, C.D., Harrison, K. and Zhou, S. (2013) Impact of land model calibration on coupled land–atmosphere prediction. *Journal of Hydrometeorology*, 14(5), 1373–1400. https://doi.org/10.1175/JHM-D-12-0127.1

Schraff, C., Reich, H., Rhodin, A., Schomburg, A., Stephan, K., Periáñez, A. and Potthast, R. (2016) Kilometre-scale ensemble data assimilation for the COSMO model (KENDA). *Quarterly Journal of the Royal Meteorological Society*, 142, 1453–1472. https://doi.org/10.1002/qj.2748. ISSN 1477-870X

Schrodin, R. and Heise, E. (2002) A new multi-layer soil model. *COSMO Newsletter*, 2(13), 149–151

Schulz, J.-P. and Vogel, G. (2020) Improving the processes in the land surface scheme TERRA: bare soil evaporation and skin temperature. *Atmosphere*, 11(5), 513–530

Schulz, J.-P., Vogel, G., Becker, C., Kothe, S., Rummel, U. and Ahrens, B. (2016) Evaluation of the ground heat flux simulated by a multi-layer land surface scheme using high-quality observations at grass land and bare soil. *Meteorologische Zeitschrift*, 25(5), 607–620. https://doi.org/10.1127/metz/2016/0537

Szunyogh, I., Kostelich, E.J., Gyarmati, G., Kalnay, E., Hunt, B.R., Ott, E., Satterfield, E. and Yorke, J.A. (2008) A local ensemble transform Kalman filter data assimilation system for the NCEP global model. *Tellus A: Dynamic Meteorology and Oceanography*, 60(1), 113–130. https://doi.org/10.1111/j.1600-0870.2007.00274.x

Tajfar, E., Bateni, S.M., Margulis, S.A., Gentine, P. and Auligne, T. (2020a) Estimation of turbulent heat fluxes via assimilation of air temperature and specific humidity into an atmospheric boundary layer model. *Journal of Hydrometeorology*, 21(2), 205–225. https://doi.org/10.1175/JHM-D-19-0104.1

Tajfar, E., Bateni, S.M., Lakshmi, V. and Ek, M. (2020b) Estimation of surface heat fluxes via variational assimilation of land surface temperature, air temperature and specific humidity into a coupled land surface-atmospheric boundary layer model. *Journal of Hydrology*, 583. https://doi.org/10.1016/j.jhydrol.2020.124577

Trigo, I.F., Monteiro, I.T., Olesen, F. and Kabsch, E. (2008) An assessment of remotely sensed land surface temperature. *Journal of Geophysical Research: Atmospheres*, 113. https://doi.org/10.1029/2008JD010035

Trigo, I.F., Dacamara, C.C., Viterbo, P., Roujean, J.-L., Olesen, F., Barroso, C., Camacho de Coca, F., Carrer, D., Freitas, S.C., García-Haro, J., Geiger, B., Gellens-Meulenberghs, F., Ghilain, N., Meliá, J., Pessanha, L., Siljamo, N. and Arboleda, A. (2011) The satellite application facility for land surface analysis. *International Journal of Remote Sensing*, 32(10), 2725–2744. https://doi.org/10.1080/01431161003743199

Trigo, I.F., Boussetta, S., Viterbo, P., Balsamo, G., Beljaars, A. and Sandu, I. (2015) Comparison of model land skin temperature with remotely sensed estimates and assessment of surface–atmosphere coupling. *Journal of Geophysical Research: Atmospheres*, 120(23), 12096–12111. https://doi.org/10.1002/2015JD023812

Viterbo, P. and Beljaars, A.C.M. (1995) An improved land surface parameterization scheme in the ECMWF model and its validation. *Journal of Climate*, 8(11), 2716–2748. https://doi.org/10.1175/1520-0442(1995)008<2716:AILSPS>2.0.CO;2

Zängl, G., Reinert, D., Rípodas, P. and Baldauf, M. (2015) The ICON (ICOsahedral non-hydrostatic) modelling framework of DWD and MPI-M: description of the non-hydrostatic dynamical core. *Quarterly Journal of the Royal Meteorological Society*, 141, 563–579. https://doi.org/10.1002/qj.2378

How to cite this article: Sgoff C, Schomburg A, Schmidli J, Potthast R. Assimilating synthetic land surface temperature in a coupled land–atmosphere model. *Q J R Meteorol Soc*. 2020;146:3980–3997. https://doi.org/10.1002/qj.3883